

# A rigorous moving wall boundary algorithm for Direct Simulation of Monte Carlo in unsteady rarefied flows

He Zhang, Fanli Shan\*, Hong Fang, Xing Zhang, Jun Zhang, Jinghua Sun

*Science and Technology on Space Physics Laboratory, Beijing 100076, P.R. China*

**Abstract:** A rigorous algorithm is proposed to improve the prediction of particle in collision with moving wall within the DSMC framework for the simulation of unsteady rarefied flows. This algorithm can predict the particle-wall collision in a coupled manner by removing the assumption employed by an approximate algorithm, in that the wall is frozen during the collision. The trajectory equation of particle is theoretically constructed in the moving object coordinate system. It can rigorously describe the geometries of the collision between particle and arbitrarily shaped object of which the motion incorporates both translation and rotation, thus allowing to deal with complex problems. In contrast, the approximate algorithm ignores the effect of moving wall on the particle movement during the collision, and therefore induces error that is an increasing function of wall velocity. Four rarefied flow problems are employed to validate the rigorous algorithm. It is shown that the rigorous algorithm can generate results perfectly consistent with the Maxwellian theoretical solutions and ensure particle conservation to avoid gas leakage. It is also shown in a 3D case of a re-entry module that the steady simulation fails to reproduce hysteresis effect while the unsteady simulation using the rigorous algorithm can do that, indicating that the unsteady simulation with an appropriate algorithm as proposed in this work is essentially required in such applications.

**Keywords:** Unsteady rarefied flow; DSMC; Moving wall boundary; Rigorous algorithm

## 1. Introduction

When the molecular mean free path ( $\lambda$ ) is comparable to or larger than the flow characteristic length scale ( $L$ ), insufficient molecular collisions will result in the gas distribution function not being maintained at the near-equilibrium state. The Knudsen number, defined as  $Kn = \lambda/L$ , is used to describe the deviation from the near-equilibrium state. For high Knudsen number flows, the strongly non-equilibrium state will affect gas transport properties, such as the viscosity and heat conduction, which results in the failure of the Navier-Stokes (NS) equations. Both rarefied and micro flows correspond to high Knudsen number. Therefore, the low orbit satellite [1,2], space vehicle [3,4], vacuum equipment [5] and micro-electro-mechanical systems (MEMS) [6,7], etc., in which rarefied or micro flow phenomena exist, are posed with problems of high Knudsen number flows.

The governing equation for high Knudsen number flows is the Boltzmann equation [8]. This equation accurately describes the temporal and spatial evolutions of the gas distribution function and the solutions can be obtained by directly solving the equation [9-11]. However, directly solving the collision term of the equation [12-15] will generate expensive computational cost,

---

\* Corresponding author at: Science and Technology on Space Physics Laboratory, Beijing 100076, P.R. China.  
E-mail address: tacyon@163.com (F. Shan).

especially when it is applied in engineering problems. In order to reduce the computational cost, some numerical schemes [16-19] that incorporate the kinetic model are proposed to simplify the computation of the collision term. These schemes make it possible to simulate high Knudsen number flows in some practical applications [19,20]. Another simplified method is to solve the asymptotic expansion equation of the Boltzmann equation. For instance, the Chapman-Enskog expansion leads to the Burnett equation [10] and the Hermite expansion leads to the grad's 13 moment equation [21]. The low-order expansion equations cannot describe strongly non-equilibrium effects and the high-order expansion equations are sensitive to numerical instabilities [22].

At present, the direct simulation Monte Carlo (DSMC) method [11] is the most widely used in simulations of high Knudsen number flows. This method has been successfully applied in a variety of studies involving rarefied or micro flows [2,5,7,22-24]. Unlike the above methods of solving partial differential equations, the DSMC method employs the Monte Carlo randomized trials to predict molecular behaviors. However, even for rarefied flows, the number of molecules is so huge that it is unaffordable to track each of them when conducting the simulation. For this reason, two simplifications are introduced to this method, aimed at reducing the amount of computation to an acceptable level. The first simplification is that each DSMC particle is regarded as a representative of a large number of molecules. The number of molecules represented by a DSMC particle is termed the scaling factor [25]. The second simplification assumes that particle movement and collisions are decoupled, in that a particle first moves in a straight line, and then collides with another. During the collision, the collision selection scheme is introduced to stochastically select two particles to form a collision pair. Among different collision selection schemes, the no time counter (NTC) scheme, proposed by Bird [26], is most popular and widely used due to its simplicity and high efficiency.

To ensure the accuracy, two conditions need to be satisfied when applying the DSMC method. First, the time step must be small compared to the mean collision time, thus allowing to decouple particle movement and collisions. This condition can be satisfied by either limiting the global time step or adopting local time step adaptation. Second, the mean distance between collision particles, termed the mean collision separation (MCS), must be limited to ensure that it is smaller than the local mean free path [11]. The generally employed strategy for limiting the MCS is to conduct the grid adaptation [27-29] or the nearest neighbor selection [30,31].

In the DSMC method, the collision between particle and wall is described by the gas-surface interaction model. The most commonly applied gas-surface interaction model is the Maxwell model [11]. This model is highly simplified due to its neglecting complex scattering characteristics of particles and thus has an advantage of easy implementation in the simulation. Other models, such as the Cercignani-Lampis-Lord (CLL) model [9], introduce additional parameters to indicate scattering characteristics, which makes them more physically realistic in comparison with the Maxwell model, but at a cost that limits their widespread use for lack of knowledge of appropriate values of the parameters.

The DSMC method was usually used to simulate steady rarefied flows in prior works. However, there exist unsteady rarefied flows involving moving walls in many engineering applications, such as separations of spacecrafts and movements of mechanisms in MEMS. Therefore, how to construct an algorithm, which is capable of dealing with moving walls, is one of essential issues in the development of the DSMC method. Bird [11] proposed a one-dimensional piston boundary algorithm and incorporated it into the DSMC method to predict shock wave formation and reflection induced by piston movement. This algorithm can be

extended to two- and three-dimensional simulations [32-35] only in the case that the motion of the wall is translational. An approximate algorithm within the DSMC framework, which assumes that the wall is stationary during the particle-wall collision, thus avoiding complex geometric computation, has also been applied for dealing with moving walls [32]. As presented in section 3, the error accumulation rate induced by this algorithm is proportional to the normal velocity of the wall. Therefore, it is appropriate to apply this algorithm in MEMS applications in which the wall moves slowly [32], but it is potentially inappropriate in spacecraft applications in which the wall may move at a high speed that tends to induce a nonnegligible error accumulation. As a result, an algorithm, which is capable of rigorously dealing with moving walls, is essentially required for the DSMC simulation. It is noted that the studies on this topic are rarefied seen in open literatures. Although complex motions incorporating translation and rotation of the wall were involved in some prior studies [36-38], mathematical details of the algorithms used were not provided. For this reason, a rigorous algorithm is proposed and detailed in the present work. This algorithm is constructed for arbitrarily shaped object of which the motion incorporates both translation and rotation. The use of the algorithm allows a rigorously geometric description of the particle-wall collision by acquiring the collision position from solving the particle trajectory equation in the moving object coordinate system, and thus essentially improves predictions of unsteady rarefied flows.

The following sections first give the stationary wall boundary condition and the approximate algorithm as well as the error analysis of this algorithm, then detail the construction of the proposed rigorous algorithm, and finally validate it in numerical studies.

## 2. Stationary wall boundary condition

Because the DSMC method assumes that particle movement and collisions are decoupled, the position of a particle after a straight-line motion within a time step is expressed as below.

$$\mathbf{P}_1 = \mathbf{P}_0 + \Delta t \mathbf{V}_0 \quad (1)$$

Here,  $\Delta t$  is the time step,  $\mathbf{P}_0$  and  $\mathbf{P}_1$  represent the particle position vectors at the moments  $t_0$  and  $t_1$  ( $t_1 = t_0 + \Delta t$ ), respectively, and  $\mathbf{V}_0$  denotes the particle velocity vector at  $t_0$ . In the case that the line segment  $\mathbf{P}_0\mathbf{P}_1$  has a geometric intersection with a stationary wall, the particle will collide with the wall and the collision moment  $t_c$  is determined as follows.

$$t_c = t_0 + \frac{|\mathbf{P}_c - \mathbf{P}_0|}{|\mathbf{P}_1 - \mathbf{P}_0|} \Delta t \quad (2)$$

Here,  $\mathbf{P}_c$  represents the collision position vector and it can be determined according to the geometric intersection between the wall and particle trajectory.

In the DSMC method, the particle reflection velocity from a wall has to be modeled. The Maxwell model, which was first used as a wall boundary condition of the Boltzmann equation, has been widely applied for determining this velocity. This model assumes that the reflection of a particle from a wall is either specular or diffusive and adopts the half Maxwellian velocity distribution [11] as presented in Eq. (3) to describe the diffusive case.

$$f_{dif}(\mathbf{V}_r) = 2 \left( \frac{m}{2\pi K T_w} \right)^{\frac{3}{2}} \exp \left( -\frac{m \mathbf{V}_r^2}{2 K T_w} \right) \quad (3)$$

Here,  $T_w$  is the wall temperature,  $m$  and  $\mathbf{V}_r$  denotes the particle mass and reflection velocity vector, respectively, and  $K$  stands for the Boltzmann constant. By presuming that the specular reflection velocity follows the Dirac delta distribution, the overall reflection velocity distribution can be obtained according to the weighted average algorithm as below.

$$f_r(\mathbf{V}_r) = (1 - \sigma_\tau) \delta(\mathbf{V}_r - \mathbf{V}_{spe}) + \sigma_\tau f_{dif}(\mathbf{V}_r) \quad (4)$$

Here,  $\sigma_\tau$  is the wall accommodation coefficient indicating the proportion of the diffusive reflection,  $\delta$  represents the Dirac delta distribution, and  $\mathbf{V}_{spe}$  denotes the specular reflection velocity vector that is determined by the incident velocity vector. After  $\mathbf{V}_r$  is obtained from Eq. (4) with a randomized sampling,  $\mathbf{P}_1$ , which incorporates the effect of the particle-wall collision, can be acquired from the following equation.

$$\mathbf{P}_1 = \mathbf{P}_c + \mathbf{V}_r (t_1 - t_c) \quad (5)$$

### 3. Approximate moving wall boundary algorithm

The boundary condition presented in section 2 is only applicable to the case of stationary wall, and it must be modified when applied to the case of moving wall. Firstly, a moving wall indicates that the particle incident velocity in the Maxwell model is no longer the particle velocity itself, but the velocity relative to the wall as shown in Eq. (6).

$$\begin{aligned} \mathbf{V}_{i, \text{Maxwell}} &= \mathbf{V}_0 - \mathbf{V}_w \\ \mathbf{V}_r &= \mathbf{V}_{r, \text{Maxwell}} + \mathbf{V}_w \end{aligned} \quad (6)$$

Here,  $\mathbf{V}_w$  denotes the wall velocity vector;  $\mathbf{V}_{i, \text{Maxwell}}$  and  $\mathbf{V}_{r, \text{Maxwell}}$  denotes respectively the incident velocity vector required by the Maxwell model and the reflection velocity vector obtained from this model. Secondly, it is more challenging to determine  $\mathbf{P}_c$  compared to the case of stationary wall. Fig. 1 illustrates an algorithm to address this issue. It freezes the wall during the particle-wall collision, and moves the wall to its new position after  $\mathbf{P}_1$  is determined. Although it is easy to implement, it is essentially an approximate algorithm and thus induces error. The analytical evaluation of the error is given in the following.

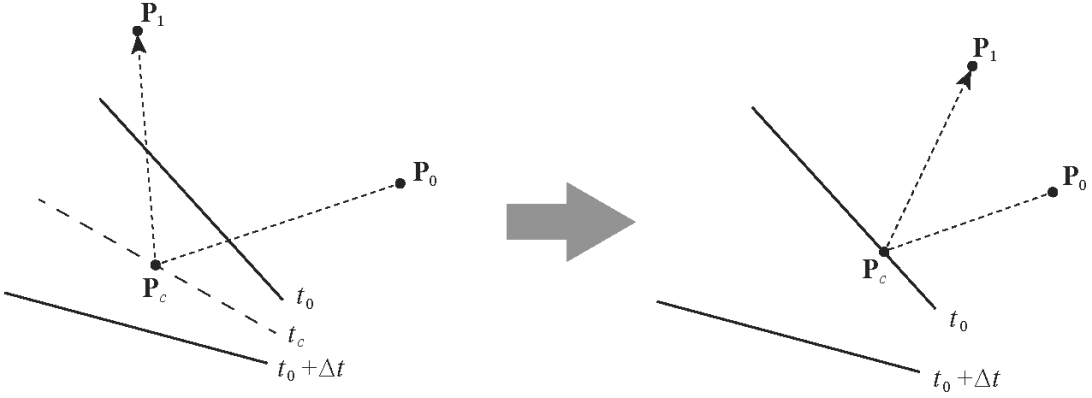


**Fig. 1.** Approximate moving wall boundary algorithm.

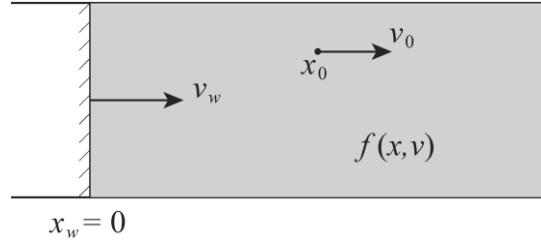


**Fig. 2.** One-dimensional moving piston.

Fig. 2 shows a one-dimensional moving piston. The velocity of the piston is  $v_w$  and the gas distribution function on the right side of the piston is  $f(x, v)$  with  $x$  and  $v$  representing the particle position and velocity. At  $t_0$ , the piston is located at  $x_w = 0$  and a particle whose velocity is  $v_0$  is located at  $x_0$ . In the premise of  $v_w > v_0$ , the collision moment  $t_c$  is determined as below.

$$t_c = t_0 + \frac{x_0}{v_w - v_0} \quad (7)$$

If the collision occurs within the time interval  $[t_0, t_1]$  ( $t_1 = t_0 + \Delta t$ ),  $x_0$  must satisfy  $0 \leq x_0 \leq (v_w - v_0)\Delta t$ . Therefore, the total number of particles that will collide with the piston within the time interval, denoted  $N_{\Delta t}$ , is expressed in the following form.

$$N_{\Delta t} = \int_{-\infty}^{v_w} \int_0^{(v_w - v)\Delta t} f(x, v) dx dv \quad (8)$$

When the approximate algorithm illustrated in Fig. 1 is applied, this number is re-expressed by Eq. (9) since the piston is frozen during the particle-wall collision, and an error, denoted  $\Delta N_{\Delta t}$ , is thus induced as shown in Eq. (10).

$$N_{\Delta t}^* = \int_{-\infty}^0 \int_0^{-v\Delta t} f(x, v) dx dv \quad (9)$$

$$\Delta N_{\Delta t} = N_{\Delta t} - N_{\Delta t}^* = \int_{-\infty}^{v_w} \int_0^{(v_w-v)\Delta t} f(x, v) dx dv - \int_{-\infty}^0 \int_0^{-v\Delta t} f(x, v) dx dv \quad (10)$$

As illustrated in Fig. 3, the integral domain of  $\Delta N_{\Delta t}$  is the region between the lines  $v = x/\Delta t$  and  $v = v_w - x/\Delta t$ , and it is divided into two parts by the  $x$  axis, indicating that Eq. (10) can be rewritten in the following form.

$$\Delta N_{\Delta t} = \int_0^{v_w} \int_0^{(v_w-v)\Delta t} f(x, v) dx dv + \int_{-\infty}^0 \int_{-v\Delta t}^{(v_w-v)\Delta t} f(x, v) dx dv \quad (11)$$

If the gas distribution is homogeneous,  $f(x, v)$  is reduced to  $f(v)$ , and thus Eq. (11) can be simplified as below.

$$\begin{aligned} \Delta N_{\Delta t} &= \Delta t \int_0^{v_w} (v_w - v) f(v) dv + v_w \Delta t \int_{-\infty}^0 f(v) dv \\ &= \Delta t \left[ \int_0^{v_w} (v_w - v) f(v) dv + v_w \int_{-\infty}^0 f(v) dv \right] \end{aligned} \quad (12)$$

By letting  $\Delta t \rightarrow 0$ , Eq. (12) can be rewritten as follows.

$$\frac{dN_{\Delta t}}{dt} = \int_0^{v_w} (v_w - v) f(v) dv + v_w \int_{-\infty}^0 f(v) dv \quad (13)$$

Here,  $dN_{\Delta t}/dt$  is the error accumulation rate of  $N_{\Delta t}$ . It is evident that this rate is dependent on  $v_w$  but independent of  $\Delta t$ . Besides,  $dN_{\Delta t}/dt$  increases with  $v_w$ . It is indicated that the error induced by the approximate algorithm cannot be reduced by shortening  $\Delta t$  and its accumulation rate will become nonnegligible if  $|v_w|$  is large. As a result, a rigorous moving wall boundary algorithm is essentially required, especially for the case of fast-moving wall.

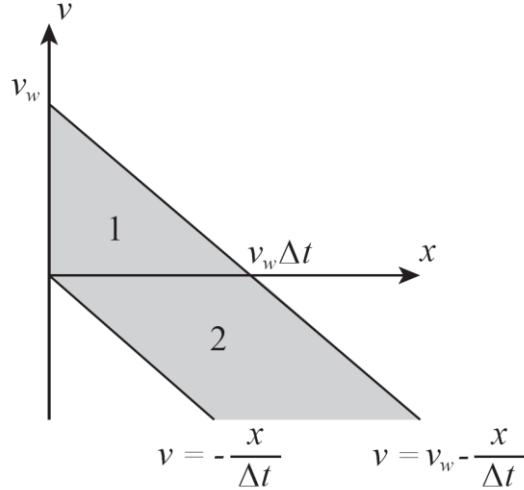


**Fig. 3.** Integral domain of  $\Delta N_{\Delta t}$  in the  $x$ - $v$  plane.

#### 4. Rigorous moving wall boundary algorithm

The key to avoid the error induced by the approximate algorithm is to rigorously determine the position of the particle-wall collision. To this end, a rigorous algorithm is proposed in the present work.

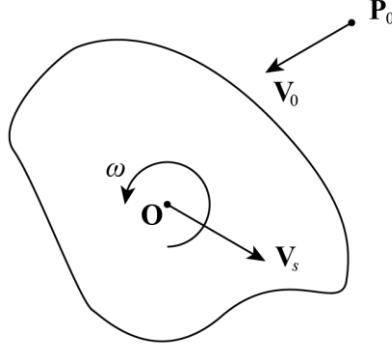


**Fig. 4.** A moving object and an incident particle.

Fig. 4 shows a moving object and an incident particle in two dimensions. At  $t_0$ , the object is translating at  $\mathbf{V}_s$  and also rotating at  $\omega$  around point  $O$ . Meanwhile, a particle located at  $P_0$  is moving in a straight line at  $\mathbf{V}_0$ . In order to facilitate determining whether the particle trajectory passes through any wall element on the surface of the object within  $[t_0, t_1]$  ( $t_1 = t_0 + \Delta t$ ), a coordinate transformation is conducted by setting the coordinate origin at  $O$ . The transformed coordinate system is denoted  $Oxy$ , and the particle position and velocity vectors in  $Oxy$  at  $t_0$ , denoted respectively  $\mathbf{P}_{0,Oxy}$  and  $\mathbf{V}_{0,Oxy}$ , are given as below.

$$\begin{aligned}\mathbf{P}_{0,Oxy} &= \mathbf{P}_0 - \mathbf{O} \\ \mathbf{V}_{0,Oxy} &= \mathbf{V}_0 - \mathbf{V}_s\end{aligned}\quad (14)$$

Here,  $\mathbf{O}$  is the position vector of  $O$  in the inertial coordinate system at  $t_0$ . Before colliding with the object, the particle trajectory in  $Oxy$  can be expressed as a function of time as shown in Eq. (15).

$$\mathbf{P}_{Oxy}(t) = \mathbf{P}_{0,Oxy} + (t - t_0) \mathbf{V}_{0,Oxy} \quad (15)$$

Here,  $\mathbf{P}_{Oxy}$  is the particle position vector in  $Oxy$  at  $t$ . As illustrated in Fig. 5, the line segment  $AB$  is a wall element on the surface of the object and its motion in  $Oxy$  is the rotation around  $O$ . There is always a point on  $AB$  or on its extension that is closest to  $O$ . This point is denoted  $O'$  and the line segment  $OO'$  is perpendicular to  $AB$ . The angle between the  $x$  axis and  $OO'$  is  $\theta$  and is a function of time as given below.

$$\theta(t) = \theta_0 + \omega(t - t_0) \quad (16)$$

Here,  $\theta_0$  is the angle at  $t_0$ . Therefore, the coordinates of  $O'$ , which are also functions of time, can be expressed in terms of  $\theta$  in the following forms.

$$\begin{aligned}x_{O'}(t) &= r \cos[\theta(t)] \\y_{O'}(t) &= r \sin[\theta(t)]\end{aligned}\quad (17)$$

Here,  $r$  is the length of  $OO'$ . By setting  $O'$  as the origin as well as setting the  $x$  and  $y$  axes in the directions of  $\overrightarrow{AB}$  and  $\overrightarrow{OO'}$ , a new coordinate system, denoted  $O'xy$ , is constructed as shown in Fig. 5. In  $O'xy$ , Eq. (15) is re-expressed as follows.

$$\mathbf{P}_{O'xy}(t) = \begin{bmatrix} \sin[\theta(t)] & -\cos[\theta(t)] \\ \cos[\theta(t)] & \sin[\theta(t)] \end{bmatrix} [\mathbf{P}_{Oxy}(t) - \mathbf{O}'] \quad (18)$$

Here,  $\mathbf{P}_{O'xy}$  is the particle position vector in  $O'xy$  at  $t$  and  $\mathbf{O}'$  is the position vector of  $O'$  in  $Oxy$  at  $t$ . Then the particle trajectory in  $O'xy$  can be determined by substituting Eqs. (14), (15) and (17) into Eq. (18). The components of the particle trajectory are given below.

$$\begin{aligned}x_{\mathbf{P}_{O'xy}}(t) &= \left\{ x_{\mathbf{P}_{Oxy}}(t) - r \sin[\theta(t)] \right\} \sin[\theta(t)] - \left\{ y_{\mathbf{P}_{Oxy}}(t) - r \cos[\theta(t)] \right\} \cos[\theta(t)] \\y_{\mathbf{P}_{O'xy}}(t) &= \left\{ x_{\mathbf{P}_{Oxy}}(t) - r \sin[\theta(t)] \right\} \cos[\theta(t)] + \left\{ y_{\mathbf{P}_{Oxy}}(t) - r \cos[\theta(t)] \right\} \sin[\theta(t)]\end{aligned}\quad (19)$$

If the particle trajectory has a geometric intersection with  $AB$ , a root of the following equation within  $[t_0, t_1]$  must exist.

$$y_{\mathbf{P}_{O'xy}}(t) = 0 \quad (20)$$

Besides, the point, corresponding to this root, must be on  $AB$ .

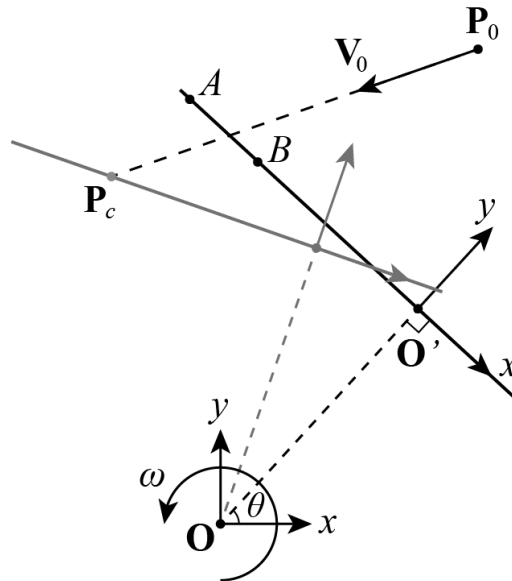


**Fig. 5.** The geometry for determining the position of the particle-wall collision.

Eq. (20) can be solved by the Newton iteration method and the solution is treated as the collision moment  $t_c$ . As long as the solution of Eq. (20) is obtained, the particle position at  $t_1$  can be rigorously determined by Eq. (5).

Although the above derivation is based on the two-dimensional case, it can be extended to three dimensions. Eq. (21) shows the expression of the vector form of the particle trajectory in three dimensions.

$$\mathbf{P}_{O'xyz}(t) = \mathbf{M} \left[ \mathbf{P}_{Oxyz}(t) - \mathbf{O}' \right] \quad (21)$$

Here,  $\mathbf{M}$  is the rotation matrix. The components of  $\mathbf{M}$  are given as follows.

$$\mathbf{M} = \begin{bmatrix} \cos \theta + (1 - \cos \theta) A_x^2 & (1 - \cos \theta) A_x A_y - \sin \theta A_z & (1 - \cos \theta) A_x A_z \sin \theta + A_y \\ (1 - \cos \theta) A_x A_y + \sin \theta A_z & \cos \theta + (1 - \cos \theta) A_y^2 & (1 - \cos \theta) A_y A_z \sin \theta - A_x \\ (1 - \cos \theta) A_x A_z - \sin \theta A_y & (1 - \cos \theta) A_y A_z + \sin \theta A_x & \cos \theta + (1 - \cos \theta) A_z^2 \end{bmatrix} \quad (22)$$

Here,  $\theta$  is the rotation angle;  $A_x$ ,  $A_y$  and  $A_z$  are the components of the unit vector of the rotation axis and all of them are the functions of time.

## 5. Results and discussions

In this section, the rigorous algorithm is validated in four rarefied flow cases. The first is the one-dimensional normal shock wave formation, the second is the flow inside a rotating square box, and the last two are unsteady hypersonic flows around a periodically rotating ellipse and the 3D Apollo Command Module.

### 5.1 One-dimensional normal shock wave formation

As shown in Fig. 2, the piston moves and compresses the gas (argon). If the velocity of the piston exceeds the local sonic speed, a normal shock wave will form in front of the piston. This is a typical unsteady problem involving a moving wall and was simulated by Bird [11] using the piston boundary algorithm within the DSMC framework.

The theoretical solutions of the post-shock state can be obtained from the Rankin-Hugoniot relations as follows.

$$\begin{aligned} \frac{\rho_2}{\rho_1} &= \frac{v_1}{v_2} = \frac{(\gamma + 1) M_a^2}{2 + (\gamma - 1) M_a^2} \\ \frac{p_2}{p_1} &= 1 + \frac{2\gamma}{\gamma + 1} (M_a^2 - 1) \\ \frac{T_2}{T_1} &= \left[ 1 + \frac{2\gamma}{\gamma + 1} (M_a^2 - 1) \right] \frac{2 + (\gamma - 1) M_a^2}{(\gamma + 1) M_a^2} \end{aligned} \quad (23)$$

Here,  $\rho$ ,  $v$ ,  $p$  and  $T$  are respectively the density, velocity, pressure and temperature, subscripts 1 and 2 indicate respectively the pre- and post-shock states,  $\gamma$  is the specific heat ratio

of gas, and  $M_a$  is the Mach number of the incoming flow. According to Eq. (23), the relation between the piston velocity  $v_w$  and the normal shock wave velocity  $v_s$  can be derived as below.

$$\frac{v_w}{v_s} = \frac{v_2 - v_1}{-v_1} = 1 - \frac{2 + (\gamma - 1)M_s^2}{(\gamma + 1)M_s^2} \quad (24)$$

Here,  $M_s$  is the Mach number corresponding to  $v_s$ . In the present work,  $v_w$ ,  $T_1$  and  $\rho_1$  are set to 1818 m/s, 273 K and  $3.34 \times 10^{-7}$  kg/m<sup>3</sup>, respectively. As a result, the moving piston will produce a Mach 8 normal shock wave according to Eq. (24).

Fig. 6. displays the temporal variations of the normalized density and temperature profiles obtained using the rigorous algorithm. The black solid line indicates the trajectory of the piston and the black dash line indicates the theoretical trajectory of the normal shock wave determined by Eq. (24). It is shown that the rigorous algorithm is able to capture the shock wave because the black dash line is located in the region where the density and temperature vary dramatically. It is also shown that the density and temperature near the piston are slightly larger than the post-shock state determined by Eq. (23). As explained by Bird [11], this is caused by an entropy layer attached to the piston, which is generated by gas passing through the incomplete normal shock wave when the piston starts to move from the stationary state.

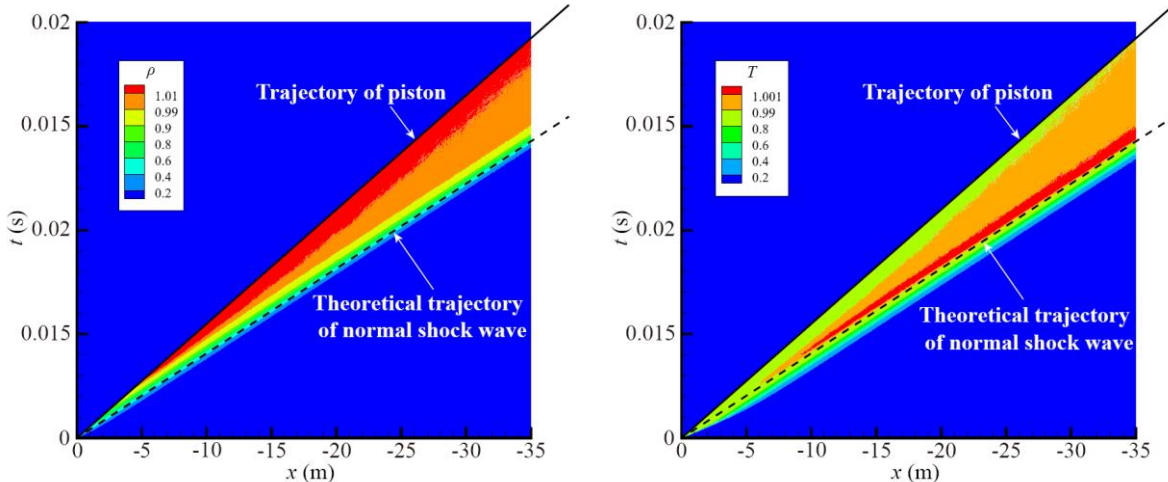


**Fig. 6.** Temporal variations of the normalized density (left) and temperature (right) profiles obtained using the rigorous algorithm for the one-dimensional normal shock wave formation.

Given in Fig. 7 are the normalized density, velocity and temperature profiles at 0.035 s. The  $x$  coordinate in this figure is nondimensionalized by the upstream mean free path  $\lambda$  that is defined in the following form.

$$\lambda = \frac{1}{\sqrt{2n\pi d^2}} \quad (25)$$

Here,  $n$  and  $d$  are respectively the number density and diameter of molecule. It is seen that the profiles are in good agreement with the Mach 8 shock wave profiles obtained using the DS1V

code [11], thus validating the rigorous algorithm on a quantitative basis. It is noted that there are slight deviations of the density and temperature at the near-wall region. This is caused by the aforementioned effect of the entropy layer.

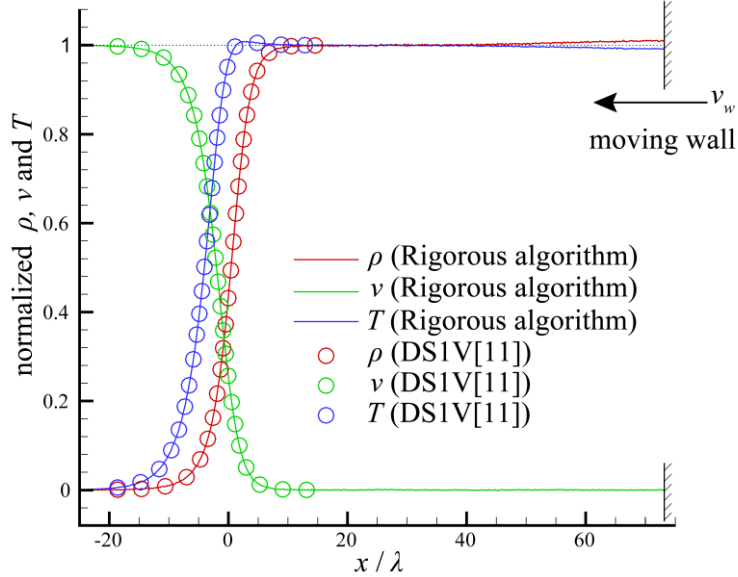


**Fig. 7.** Normalized density, velocity and temperature profiles at 0.035 s for the one-dimensional normal shock wave formation.

It is noted that the one-dimensional piston boundary algorithm [11] is the reduced case of the rigorous algorithm and is able to accurately describe the particle-wall collision in cases involving only translational motion. However, it is unable to deal with cases involving rotational motion, while the rigorous algorithm, in contrast, is able to do that as shown in the following sections.

## 5.2 Rotating square box

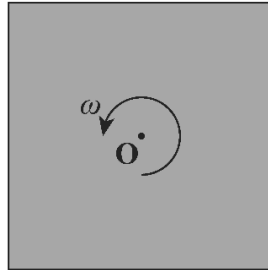


**Fig. 8.** Rotating square box.

Fig. 8 shows a square box rotating around its center at  $50\pi$  rad/s. The side length, the wall temperature and the wall accommodation coefficient of the box are 5 m, 273 K and 1, respectively. At the beginning, the gas (argon) is homogeneously distributed inside the box and its density and temperature are respectively  $3.34 \times 10^{-7}$  kg/m<sup>3</sup> and 273 K. After a sufficient time, the gas rotates in equilibrium. Maxwell [39] proposed a relation, as shown in Eq. (26), to describe the gas distribution at the equilibrium state for this rotating case.

$$f(x, y, u, v, w) = \rho_O \left( \frac{m}{2\pi K T_O} \right)^{\frac{3}{2}} \exp \left\{ -\frac{m}{2 K T_O} \left[ u^2 + v^2 + w^2 + 2\omega(u y - v x) \right] \right\} \quad (26)$$

Here,  $\omega$  is the angular velocity of the box;  $\rho_O$  and  $T_O$  are respectively the density and temperature at point  $O$  that is at the center of the box;  $u$ ,  $v$  and  $w$  are respectively the  $x$ ,  $y$  and  $z$ -direction velocities of molecules. By integrating Eq. (26), the distributions of the density  $\rho(x, y)$  and temperature  $T(x, y)$  as well as velocities  $U(x, y)$  and  $V(x, y)$  at the equilibrium state are determined as follows.

$$\begin{aligned} \rho(x, y) &= \int_{-\infty}^{\infty} \int_{-\infty}^{\infty} \int_{-\infty}^{\infty} f(x, y, u, v, w) du dv dw = \rho_O \exp \left[ \frac{m\omega^2}{2 K T_O} (x^2 + y^2) \right] \\ T(x, y) &= \frac{1}{\rho} \int_{-\infty}^{\infty} \int_{-\infty}^{\infty} \int_{-\infty}^{\infty} \left[ (u - U)^2 + (v - V)^2 + w^2 \right] \frac{m}{3k} f(x, y, u, v, w) du dv dw = T_O \\ U(x, y) &= \frac{1}{\rho} \int_{-\infty}^{\infty} \int_{-\infty}^{\infty} \int_{-\infty}^{\infty} u f(x, y, u, v, w) du dv dw = -\omega y \\ V(x, y) &= \frac{1}{\rho} \int_{-\infty}^{\infty} \int_{-\infty}^{\infty} \int_{-\infty}^{\infty} v f(x, y, u, v, w) du dv dw = \omega x \end{aligned} \quad (27)$$

It is indicated by Eq. (27) that the gas is stationary relative to the box and has a spatially uniform temperature distribution at the equilibrium state. Due to the conservation of mass, the spatial integral of  $\rho(x, y)$  satisfies the following equation.

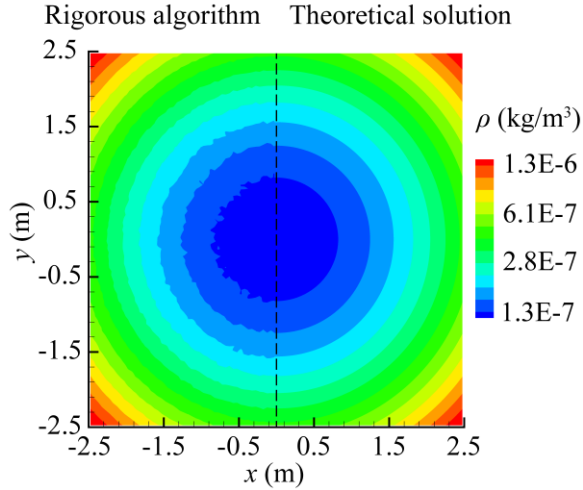
$$\int_{-l/2}^{l/2} \int_{-l/2}^{l/2} \rho_O \exp \left[ \frac{m\omega^2}{2 K T_O} (x^2 + y^2) \right] dx dy = \rho_0 l^2 \quad (28)$$

Here,  $l$  is the side length of the box and  $\rho_0$  is the uniform density of the gas at the beginning. By solving Eq. (28),  $\rho_O$  is obtained as given below.

$$\rho_O = \frac{m \rho_0 l^2 \omega^2}{4\pi K T \left[ \operatorname{erfi} \left( \sqrt{\frac{ml^2 \omega^2}{8KT}} \right) \right]^2} = 1.136 \times 10^{-7} \text{ kg/m}^3 \quad (29)$$

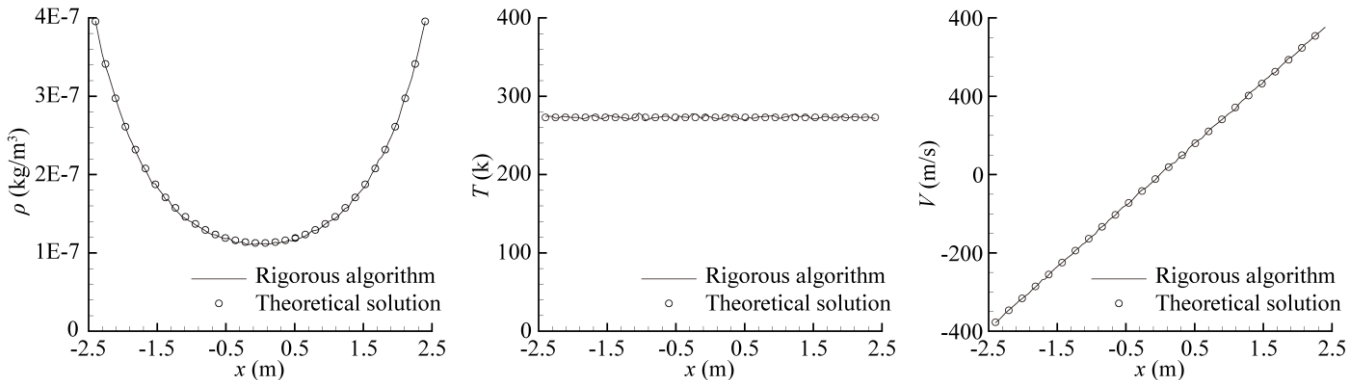
Here,  $\operatorname{erfi}$  indicates the imaginary error function.

Fig. 9 displays the equilibrium density distribution of the present simulation using the rigorous algorithm (on the left side of the black dash line) compared with the Maxwellian theoretical solution determined by Eq. (27) (on the right side of the black dash line). It is clearly seen that the simulated result agrees well with the theoretical solution.



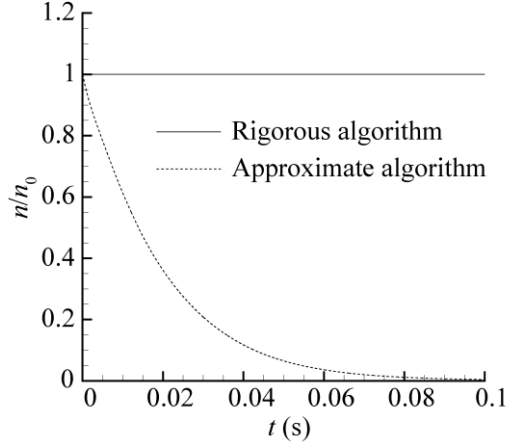
**Fig. 9.** The equilibrium density distribution inside the rotating square box.

Fig. 10 summarizes and compares the profiles of the equilibrium density, temperature and  $y$ -direction velocity at  $y = 0$  between the results generated by the rigorous algorithm and the Maxwellian theoretical solutions. It can be seen that the rigorous algorithm is able to generate results that are perfectly consistent with the theoretical solutions. In addition, the temperature of the present simulation at  $y = 0$  is approximately 273 K, thus conforming the fact that the temperature distribution at the equilibrium state is uniform.



**Fig. 10.** The profiles of the equilibrium density (left), temperature (middle) and  $y$ -direction velocity (right) at  $y = 0$  inside the rotating square box.

Because the approximate algorithm decouples the motions of wall and particles by freezing the wall during the particle-wall collision, it cannot identify each collision and tends to induce particles to penetrate the wall and thus leads to gas leakage. In contrast, the rigorous algorithm takes the effect of the wall's motion into consideration during the collision and accurately determines the collision moment and position, and thus the gas leakage can be avoided. Fig. 11 shows the comparison between the approximate and rigorous algorithms in the prediction of the particle number inside the box. It is evident that the rigorous algorithm ensures the particle conservation, while the approximate algorithm induces gas leakage, in that the particles almost vanish from the box after 0.1 s (20,000 time steps).



**Fig. 11.** The temporal variation of the particle number inside the rotating square box.

### 5.3 Periodically rotating ellipse



**Fig. 12.** Periodically rotating ellipse.

In order to validate the rigorous algorithm in complex problems, a periodically rotating ellipse as shown in Fig. 12 is employed in this work. The ellipse rotates around its center in a Mach 8 flow (argon) and its rotation angle  $\theta$  is a sinusoidal function of time as given below.

$$\theta = \theta_{\max} \sin(2\pi f_p t) \quad (30)$$

Here,  $f_p$  is the rotation frequency;  $\theta_{\max}$  is the rotation amplitude and is set to  $45^\circ$ . The lengths of the long and short axes of the ellipse are 6 and 3 m, respectively. The wall temperature is 273 K and the wall accommodation coefficient is 0.8. The density and temperature of the incoming flow are respectively  $3.34 \times 10^{-7}$  kg/m<sup>3</sup> and 273 K.

Fig. 13 and Fig. 14 display the simulated pressure distributions at  $f_p = 31.25$  and 125 Hz, respectively. It is noted that the approximate algorithm tends to generate lower pressure in front of the ellipse compared to the rigorous algorithm. The maximum pressures at different moments for the two algorithms are shown in Table 1, where  $t_p$  is the rotation time period. For the case of 31.25 Hz, it is seen that the maximum pressure at  $t = 0$  and  $0.125t_p$  predicted by the approximate algorithm are respectively 5.5% and 1.2% lower than that by the rigorous algorithm. This is an inevitable result since the approximate algorithm is unable to accurately determine the position of the particle-wall collision with the frozen-wall assumption, which induces particles to penetrate the wall and thus leads to pressure decrease. For the case of 125 Hz, the pressure decrease becomes more sever. It is consistent with the indication of Eq. (13) in section 3, in that the error induced by the approximate algorithm grows as the wall velocity is increased.

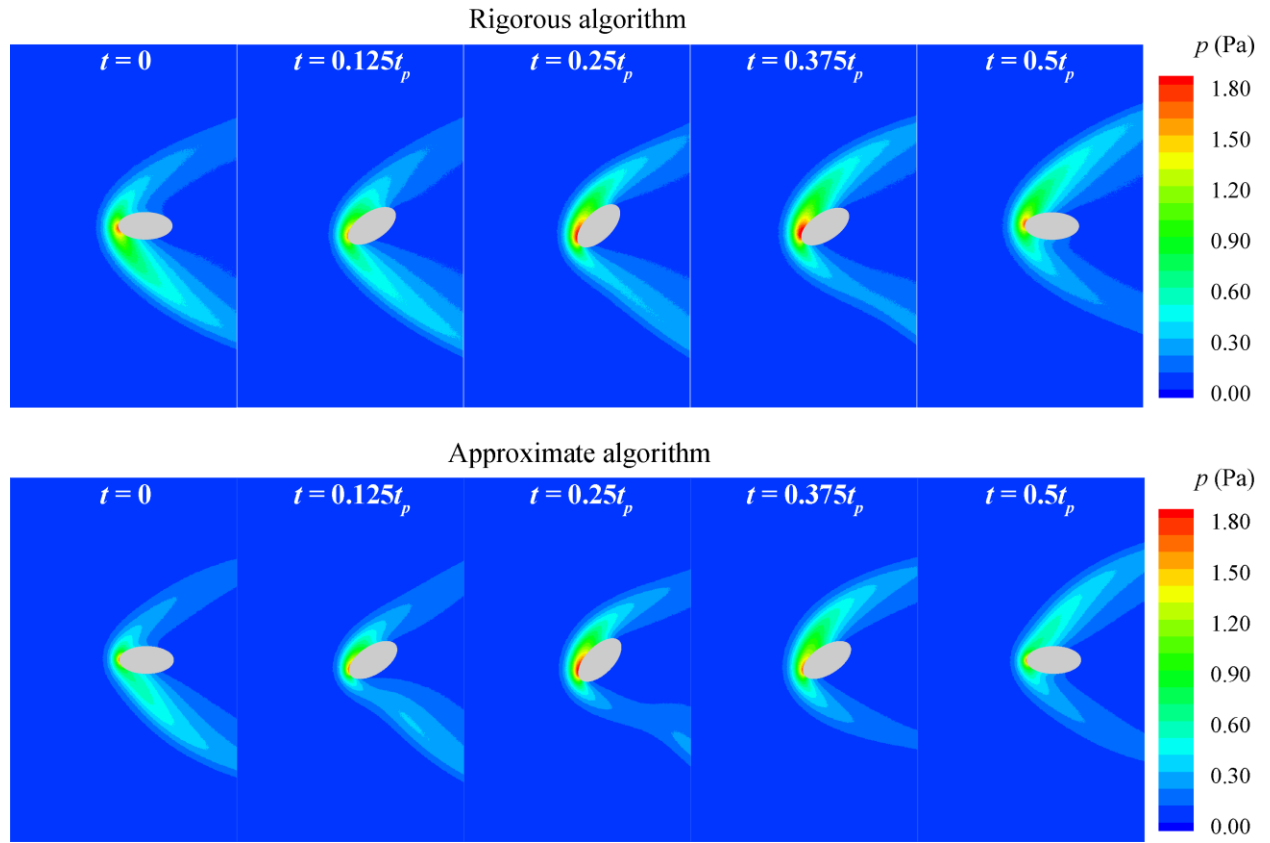


**Fig. 13.** The pressure distributions obtained using the rigorous (top) and approximate (bottom) algorithms for the periodically rotating ellipse ( $f_p = 31.25$  Hz).

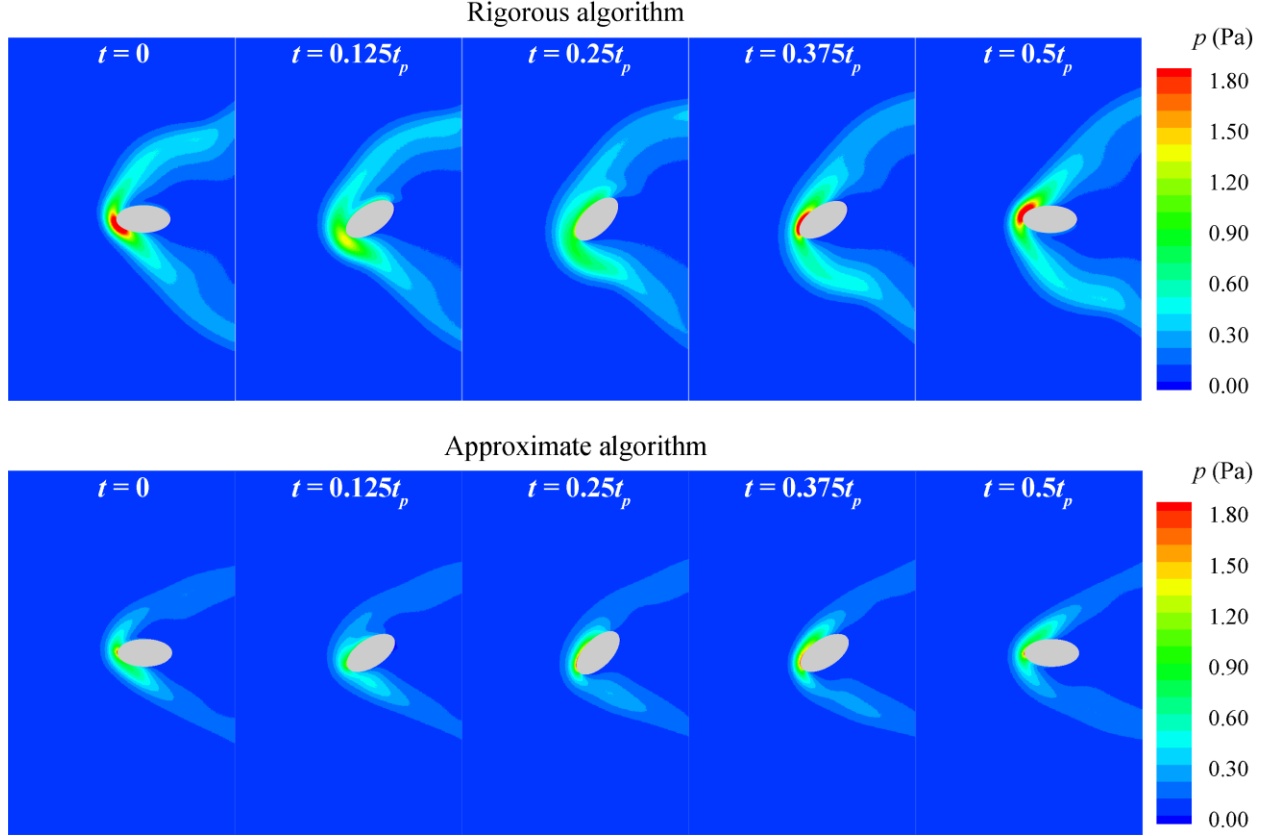


**Fig. 14.** The pressure distributions obtained using the rigorous (top) and approximate (bottom) algorithms for the periodically rotating ellipse ( $f_p = 125$  Hz).

**Table 1.** The maximum pressure obtained using the rigorous and approximate algorithms for the periodically rotating ellipse.

$f_p$ (Hz)	$t$ (s)	Maximum pressure (Pa)		Deviation (%)	
		Rigorous algorithm	Approximate algorithm		
31.25	0	1.83	1.73	5.5	
	$0.125t_p$	1.67	1.65	1.2	
125	0	2.84	1.84	35.2	
	$0.125t_p$	1.43	1.15	19.6	

The gas leakage induced by the approximate algorithm is revealed by the particle distributions in Fig. 15 and Fig. 16. Only 1/1000 of the particles are shown in the figures. It is evident that the approximate algorithm induces particles to penetrate the rotating wall and enter the ellipse. Furthermore, more particles enter the ellipse at the higher rotation frequency (125 Hz), indicating a more severe gas leakage. In contrast, the rigorous algorithm ensures that the particle-wall collision is accurately predicted and thus avoid gas leakage.

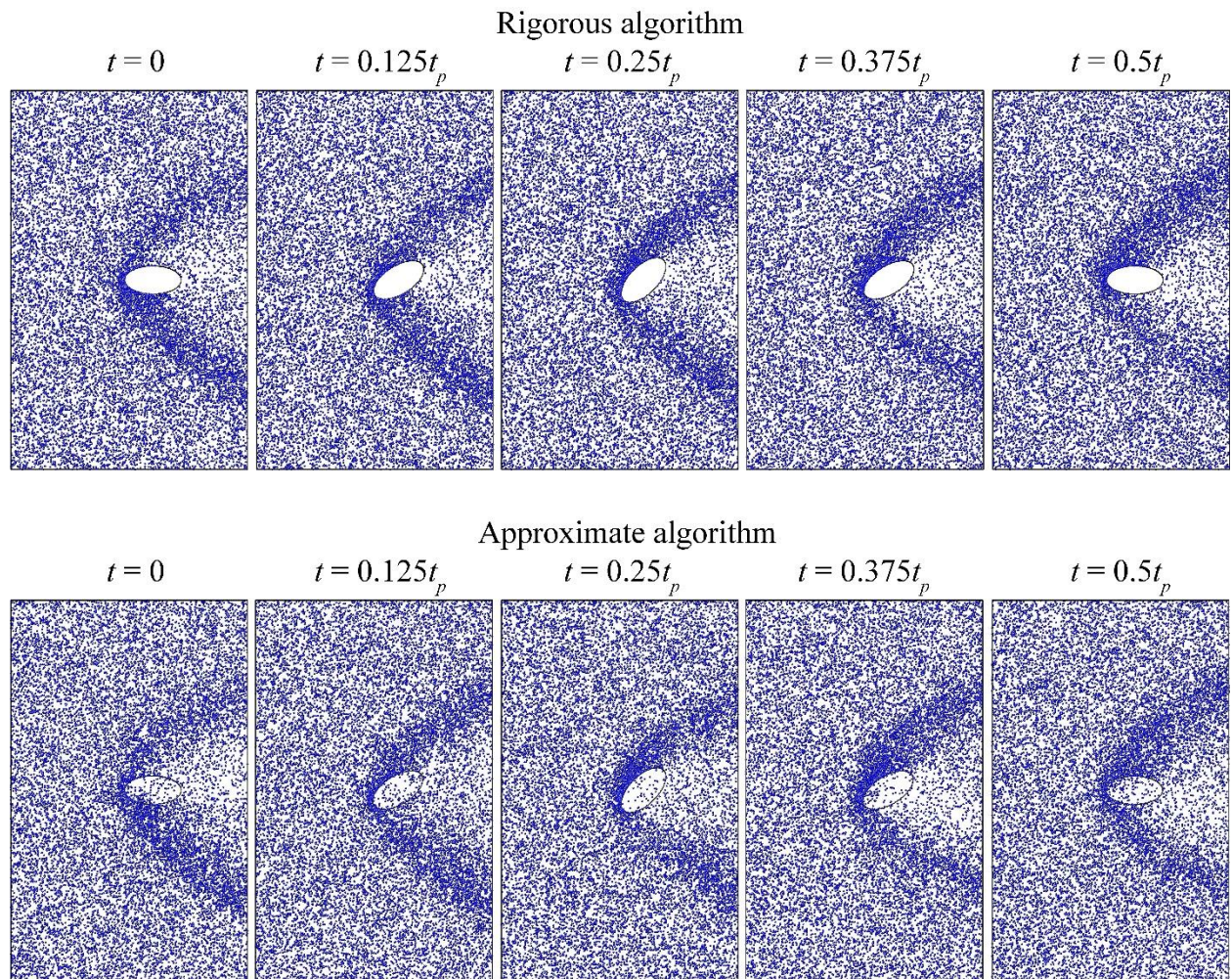


**Fig. 15.** The particle distributions obtained using the rigorous (top) and approximate (bottom) algorithms for the periodically rotating ellipse ( $f_p = 31.25$  Hz).

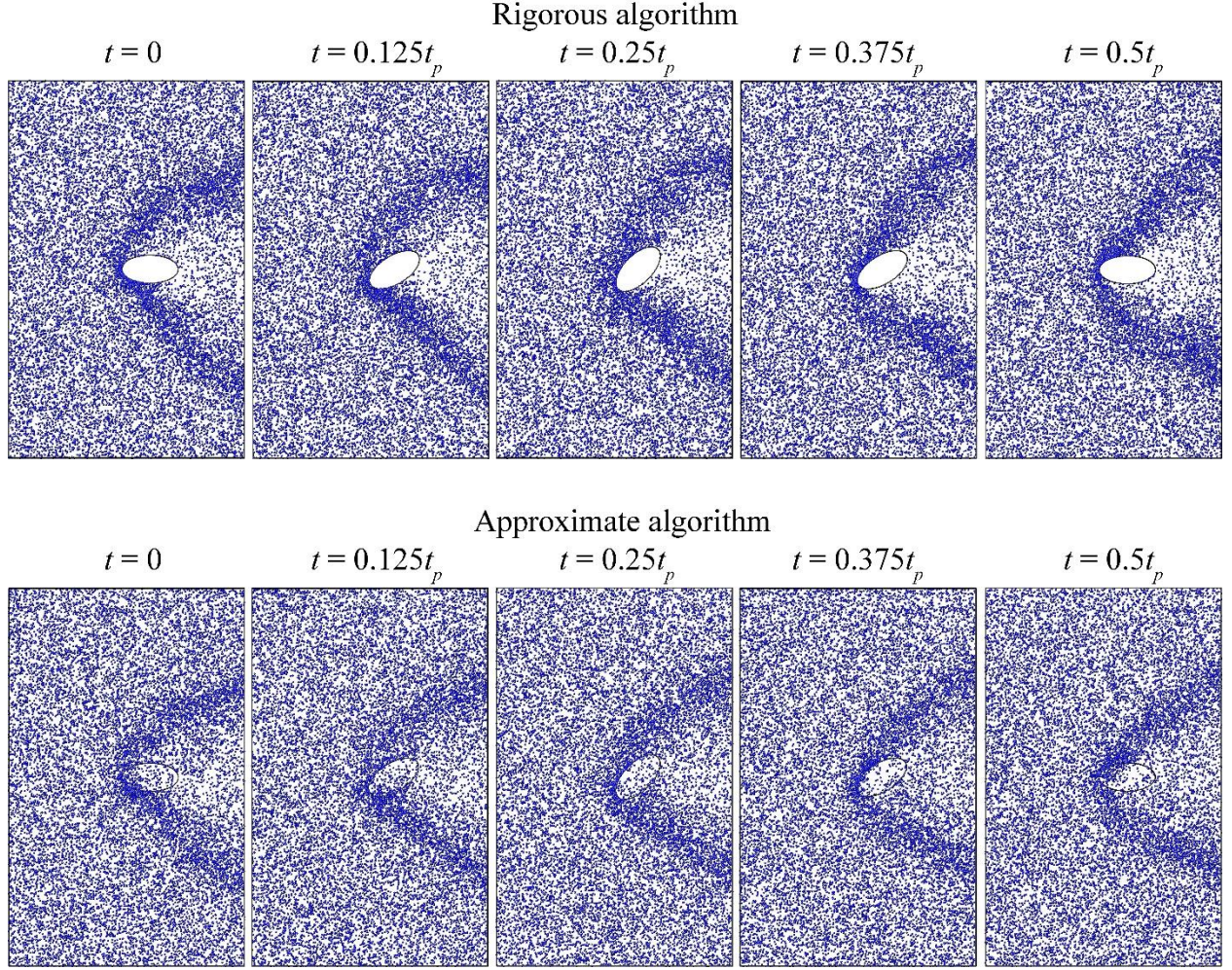


**Fig. 16.** The particle distributions obtained using the rigorous (top) and approximate (bottom) algorithms for the periodically rotating ellipse ( $f_p = 125$  Hz).

#### 5.4 3D Apollo Command Module

The re-entry module is a typical space vehicle that travels through the rarefied atmosphere at a speed of thousands of meters per second. The Apollo command Module (ACM) is one of the most famous re-entry modules and is widely adopted as a benchmark case for numerical validation. In this work, the ACM [40] is employed to validate the rigorous algorithm in three dimensions.

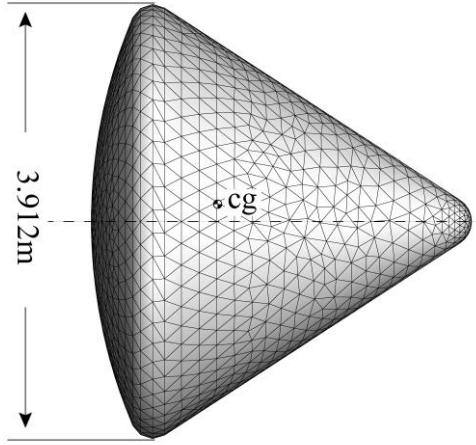


**Fig. 17.** The axisymmetric view of the ACM geometry and surface grids.

Fig. 17 shows the axisymmetric view of the ACM geometry and surface grids. The ACM rotates around its center of gravity (cg) in the X-Y centerplane in a Mach 10.2 flow (nitrogen) that corresponds to  $Kn_{\infty} = 0.067$ . The temperature of the incoming flow is 142.2 K. In the present simulation, the variation of the rotation angle  $\theta$  also follows the sinusoidal function shown in Eq. (30), in which  $f_p$  and  $\theta_{\max}$  are respectively set to 156.25 Hz and 30°.

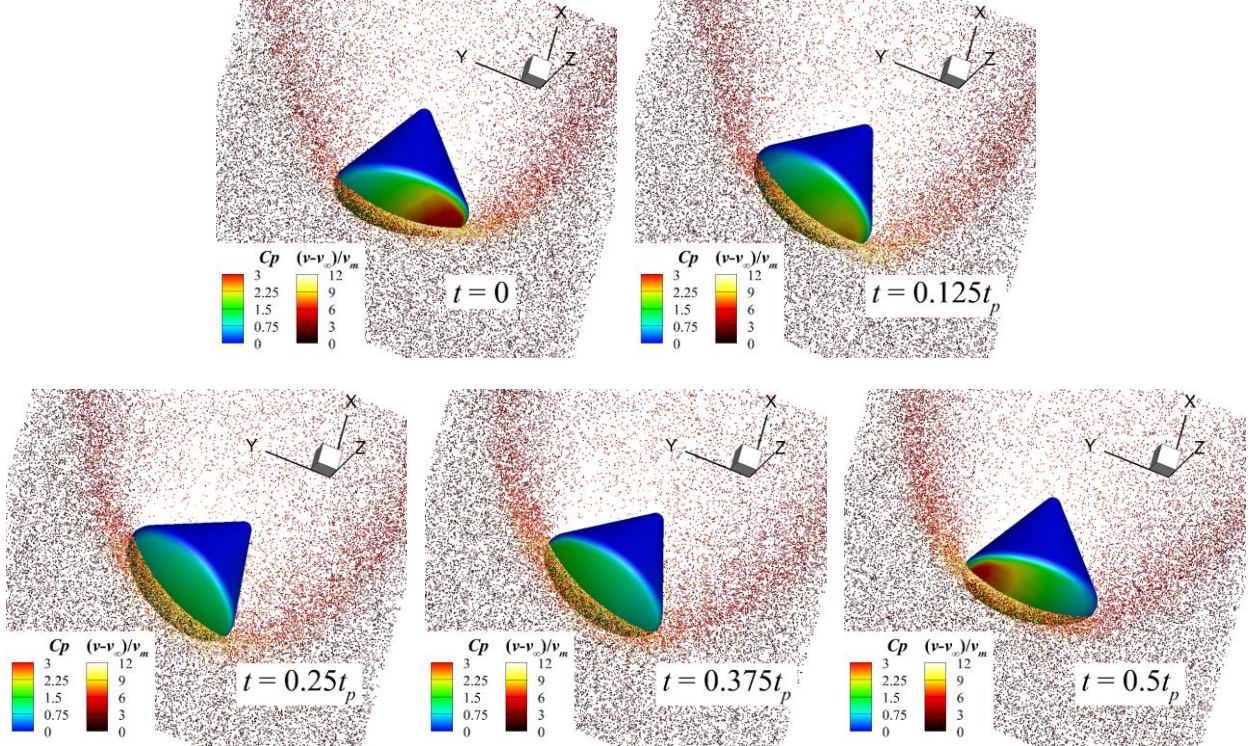


**Fig. 18.** The surface pressure coefficient distributions and particle distributions in the X-Y centerplane obtained using the rigorous algorithm for the ACM.

The surface pressure coefficient distributions in half time period predicted by the rigorous algorithm are displayed in Fig. 18. The particle distributions in the X-Y centerplane, colored by  $(v - v_\infty)/v_m$  with  $v_m = \sqrt{3KT_\infty/m}$  representing the molecular mean velocity of the incoming flow, are also displayed in the figure. It is noted that both surface pressure coefficient and particle distributions at  $t = 0$  are noticeably different from that at  $t = 0.5t_p$ , though the ACM is in the same attitude at the two moments, indicating that the flow is highly unsteady.

Fig. 19 shows the variations of the lift and drag coefficients in terms of the rotation angle and compares the results of the unsteady and steady simulations. It is seen that the steady result obtained in the present work is very close to that obtained in a prior work of Padilla et al. [40] with the use of a DSMC solver MONAGO. Besides, the unsteady result obtained using the rigorous algorithm illustrates a noticeable hysteresis effect that is characterized by the hysteresis loops of the lift and drag coefficients. This result is significantly different from the steady one. It is indicated that the steady simulation may cause a failure in predictions of lift and drag coefficients in practical unsteady problems and thus an unsteady simulation with an appropriate algorithm as proposed in this work is essentially required. It is also seen that the hysteresis loops are asymmetric about  $\theta = 0^\circ$ . This is because the ACM rotates around its center of gravity that is not on the geometric central line as shown in Fig. 17.

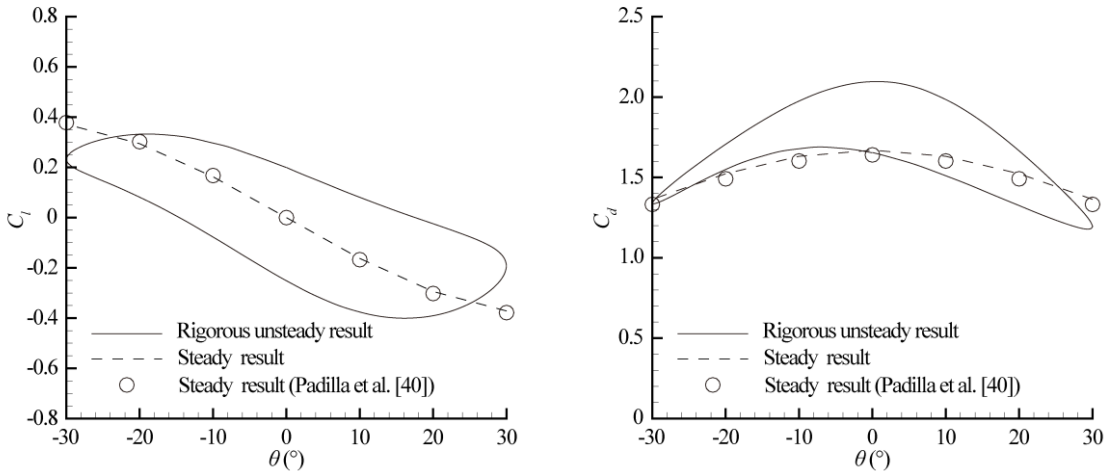


**Fig. 19.** The lift (left) and drag (right) coefficients in terms of the rotation angle for the ACM.

## 6. Conclusions

In this work, a rigorous algorithm, aimed at dealing with moving walls within the DSMC framework, is proposed and validated in rarefied flow problems.

- 1) The rigorous algorithm removes the frozen-wall assumption that is employed by an approximate algorithm, thus allowing to predict the particle-wall collision in a coupled manner.
- 2) By theoretically constructing the trajectory equation of particle in collision with arbitrarily shaped object of which the motion incorporates both translation and rotation, the moment and position of the particle-wall collision can be accurately determined.
- 3) The error analysis is conducted for the approximate algorithm. It is revealed that the error induced by this algorithm is proportional to the wall velocity, indicating that the error is nonnegligible if the wall moves at a high speed.

4) It is shown that the rigorous algorithm is able to capture the one-dimensional normal shock wave induced by moving piston, reproduce the equilibrium state inside the rotating square box, and characterize the unsteady rarefied hypersonic flows around the periodically rotating ellipse and ACM. The simulated results are perfectly consistent with the Maxwellian theoretical solutions. Besides, this algorithm essentially ensures the particle conservation by accurately predicting the particle-wall collision and thus avoid gas leakage. The approximate algorithm, in contrast, tends to induce gas leakage since it freezes the wall during the collision. Both the theoretical expression and simulated results indicate that the gas leakage induced by the approximate algorithm gets more sever as the wall velocity is increased. It is also shown in the ACM case that the unsteady simulation with an appropriate algorithm as proposed in this work is essentially required for reproducing the hysteresis effect in such applications.

## Acknowledgements

The financial assistances provided by the National Key Research and Development Program of China (No. 2019YFB1704204) is gratefully acknowledged.

## References

- [1] K. Fujita, A. Noda, Rarefied aerodynamics of a super low altitude test satellite, in: 41st AIAA Thermophysics Conference, 2009, p. 3606.
- [2] K. H. Lee, S. W. Choi, Interaction effect analysis of thruster plume on LEO satellite surface using parallel DSMC method, *Computers & Fluids* 80 (2013) 333–341.
- [3] J. Maus, B. Griffith, K. Szema, J. Best, Hypersonic Mach number and real gas effects on space shuttle orbiter aerodynamics, *Journal of Spacecraft and Rockets* 21 (2) (1984) 136–141.
- [4] C. C. Kiris, J. A. Housman, M. F. Barad, C. Brehm, E. Sozer, S. Moiniyekta, Computational framework for launch, ascent, and vehicle aerodynamics (LAVA), *Aerospace Science and Technology* 55 (2016) 189–219.
- [5] X. Luo, C. Day, V. Hauer, O. Malyshev, R. Reid, F. Sharipov, Monte Carlo simulation of gas flow through the KATRIN DPS2-F differential pumping system, *Vacuum* 80 (8) (2006) 864–869.
- [6] S. Shoji, M. Esashi, Microflow devices and systems, *Journal of Micromechanics and Microengineering* 4 (4) (1994) 157–171.
- [7] H. Akhlaghi, E. Roohi, S. Stefanov, A new iterative wall heat flux specifying technique in DSMC for heating/cooling simulations of MEMS/NEMS, *International Journal of Thermal Sciences* 59 (2012) 111–125.
- [8] L. Boltzmann, Weitere Studien über das Wärmegleichgewicht unter Gasmolekülen, *Sitzungsberichte Akademie der Wissenschaften* 66 (1872) 275–370.
- [9] C. Cercignani, The Boltzmann equation and its applications, Springer Verlag New York, 1988.
- [10] S. Chapman, T. G. Cowling, The mathematical theory of non-uniform gases, Cambridge University Press 1939.
- [11] G. Bird, Molecular gas dynamics and the direct simulation of gas flows, Oxford University Press, 1994.
- [12] V. V. Aristov, Direct methods for solving the Boltzmann equation and study of nonequilibrium flows, Kluwer Academic Publishers, 2001.

- [13] L. Yang, C. Shu, W. Yang, Z. Chen, H. Dong, An improved discrete velocity method (DVM) for efficient simulation of flows in all flow regimes, *Physics of Fluids* 30 (6) (2018) 062005.
- [14] L. Wu, C. White, T. J. Scanlon, J. M. Reese, Y. Zhang, Deterministic numerical solutions of the Boltzmann equation using the fast spectral method, *Journal of Computational Physics* 250 (2013) 27–52.
- [15] I. M. Gamba, J. R. Haack, C. D. Hauck, J. Hu, A fast spectral method for the Boltzmann collision operator with general collision kernels, *SIAM Journal on Scientific Computing* 39 (4) (2017) B658–B674.
- [16] K. Xu, J. C. Huang, A unified gas-kinetic scheme for continuum and rarefied flows, *Journal of Computational Physics* 229 (20) (2010) 7747–7764.
- [17] Z. Guo, K. Xu, R. Wang, Discrete unified gas kinetic scheme for all Knudsen number flows: Low-speed isothermal case. *Physical Review E* 88 (3) (2013) 033305-033305.
- [18] C. Liu, Y. Zhu, K. Xu, Unified gas-kinetic wave-particle methods I: Continuum and rarefied gas flow, *Journal of Computational Physics* 401 (2020) 108977.
- [19] Z. Li, H. Zhang, Gas-kinetic numerical studies of three-dimensional complex flows on spacecraft re-entry, *Journal of Computational Physics* 228 (4) (2009) 1116–1138.
- [20] A. Peng, Z. Li, J. Wu, X. Jiang, Implicit gas-kinetic unified algorithm based on multi-block docking grid for multi-body reentry flows covering all flow regimes, *Journal of Computational Physics* 327 (2016) 919–942.
- [21] H. Grad, On the kinetic theory of rarefied gases, *Communications on pure and applied mathematics* 2 (4) (1949) 331–407.
- [22] E. Josyula, J. Burt, Review of rarefied gas effects in hypersonic applications, Tech. rep., AIR FORCE RESEARCH LAB WRIGHTPATTERSON AFB OH (2011).
- [23] G. J. LeBeau, F. E. Lumpkin III, Application highlights of the DSMC analysis code (DAC) software for simulating rarefied flows, *Computer Methods in Applied Mechanics and Engineering* 191 (6-7) (2001) 595–609.
- [24] O. Aktas, N. R. Aluru, U. Ravaioli, Application of a parallel DSMC technique to predict flow characteristics in microfluidic filters, *Journal of Microelectromechanical Systems* 10 (4) (2001) 538–549.
- [25] Z. Sun, Z. Tang, Y. He, W. Tao, Proper cell dimension and number of particles per cell for DSMC, *Computers & Fluids* 50 (1) (2011) 1–9.
- [26] G.A. Bird, The perception of numerical methods in rarefied gas dynamics, in: 16th Int. Sym. on Rarefied Gas Dynamics, 1989, p. 211.
- [27] C. Su, K. Tseng, H. Cave, J. Wu, Y. Lian, T. Kuo, M. Jermy, Implementation of a transient adaptive sub-cell module for the parallel-DSMC code using unstructured grids, *Computers & Fluids* 39 (7) (2010) 1136–1145.
- [28] M. G. Kim, H. S. Kim, O. J. Kwon, A parallel cell-based DSMC method on unstructured adaptive meshes, *International journal for numerical methods in fluids* 44 (12) (2004) 1317–1335.
- [29] G. LeBeau, K. Jacikas, F. Lumpkin, Virtual sub-cells for the direct simulation Monte Carlo method, in: 41st Aerospace Sciences Meeting and Exhibit, 2003, p. 1031.
- [30] M. N. Macrossan, Searching for a near neighbor particle in DSMC cells using pseudo-subcells, *Journal of Computational Physics* 229 (17) (2010) 5857–5861.
- [31] M. Gallis, J. Torczynski, Effect of collision-partner selection schemes on the accuracy and efficiency of the direct simulation Monte Carlo method, *International journal for numerical*

methods in fluids 67 (8) (2011) 1057–1072.

- [32] D. Rader, M. Gallis, J. Torczynski, DSMC moving-boundary algorithms for simulating mems geometries with opening and closing gaps, in: 27th International Symposium on Rarefied Gas Dynamics, 2011, pp. 760–765.
- [33] R. Versluis, R. Dorsman, L. Thielen, M. Roos, Numerical investigation of turbomolecular pumps using the direct simulation Monte Carlo method with moving surfaces, *Journal of Vacuum Science & Technology A: Vacuum, Surfaces, and Films* 27 (3) (2009) 543–547.
- [34] N. Sengil, F. Edis, Implementation of parallel DSMC method to adiabatic piston problem, in: *Parallel Computational Fluid Dynamics 2007*, Springer, 2009, pp. 75–82.
- [35] S. Stefanov, R. Barber, M. Ota, D. Emerson, Comparison between Navier-Stokes and DSMC calculations for low Reynolds number slip flow past a confined microsphere, in: 24th International Symposium on Rarefied Gas Dynamics, 2005, pp. 701–706.
- [36] W. Jin, J. R. van Ommen, C. R. Kleijn, A new cut-cell algorithm for DSMC simulations of rarefied gas flows around immersed moving objects, *Computer Physics Communications* 212 (2017) 146–151.
- [37] S. Shrestha, S. Tiwari, A. Klar, S. Hardt, Numerical simulation of a moving rigid body in a rarefied gas, *Journal of Computational Physics* 292 (2015) 239–252.
- [38] M. Shamseddine, I. Lakkis, A novel spatio-temporally adaptive parallel three-dimensional DSMC solver for unsteady rarefied micro/nano gas flows, *Computers & Fluids* 186 (2019) 1–14.
- [39] J. Maxwell, A Treatise on the Kinetic Theory of Gases, *Nature* 16 (1877) 242–246.
- [40] J. Padilla, I. Boyd, Assessment of gas-surface interaction models in DSMC analysis of rarefied hypersonic flow, in: *AIAA Thermophysics Conference*, 2013.